A Partial Coherent Interferometry for measuring the thickness of a dynamic liquid sheet

Weixiao Shang, Jun Chen*

School of Mechanical Engineering, Purdue University, 585 Purdue Mall, West Lafayette, IN 47907, United States

ARTICLE INFO

ABSTRACT

This work presents a non-invasive technique, Partial Coherent Interferometry, for measuring the thickness distribution of a dynamic liquid sheet. It utilizes the linear relationship between the degree of coherence and the optical path difference to determine the thickness of the sheet. In an interferometer using a partial coherent laser, the interference patterns before and after the liquid sheet insertion are digitally recorded. The relative thickness distribution is determined by applying a phase unwrapping process to the recorded interference pattern. By measuring the change of the degree of coherence introduced by the sheet, the absolute thicknesses at the reference points are determined. By matching the relative thickness to the absolute thicknesses at different points, the absolute thickness distribution is retrieved. To verify the reliability of this method, a glass sample and a static ethanol film, both with nominal thicknesses (152.4 μm), are measured first. The results, a nearly uniform thickness of 148.8 ± 1.8 μm for glass and a varying thickness distribution around 154.6 μm for static ethanol film, show the capability of this method to measure a two-dimensional thickness distribution of a thin liquid sheet. Then a dynamic impinging sheet formed by the two ethanol jets with Reynolds number 763 and Weber number 143 is measured by Partial Coherent Interferometry. The thickness distribution ranges from 26 to 38 μm with an uncertainty of 2.1 μm.

© 2019 Elsevier Ltd. All rights reserved.

1. Introduction

Liquid sheets formed by jets collision are frequently observed in the atomizer of propulsion systems (e.g., the fuel injector of rocket engines), the cooling systems (e.g., the cooling spray for the roller in the hot mill), and many other applications in chemical engineering systems or energy production systems (Sutton and Biblarz, 2017; Bayvel, 1993; Chojnacki, 1997; Shiina et al., 2000). In most of these applications, it is the essential function of the impinging jets atomizers to generate the droplets with the appropriate size efficiently. A thin liquid sheet is first formed around the impinging point by the impingement of the jets. Then, under the combined influences of surface tension, viscous force, inertial force, and aerodynamic force, the sheet is destabilized and eventually breaks up into ligaments and droplets at the downstream (Kang et al., 1995). Thus, characterizing the impinging sheet is important for understanding the underlying physics and the model development. Among the different quantitative parameters, the thickness of the impinging sheet acts as a key one in the existing theoretical models (Miller, 1960; Taylor, 1960; Hasson and Peck, 1964; Couto and Bastos-Netto, 1991; Li and Ashgriz, 2006). A correct measurement of the sheet thickness could give the guidance to high-fidelity numerical simulations about the needed resolution for resolving the sheet structures. However, the challenge remains when one tries to measure the thickness of this kind of dynamic sheet.

The measurements of liquid sheet can be classified as invasive methods and non-invasive methods. The invasive methods determine the liquid thickness by measuring the liquid conductivity via contact probes (Fukano, 1998; de Jong and Gabriel, 2003). Since the contact between probes and liquid changes the local thickness distribution and the velocity field, or even breaks the liquid structure, this kind of methods are usually applied only in large-scale measurements. On the other hand, the non-invasive methods determine the liquid thickness without a physical contact to the sheet. While a few techniques use ultrasound (Fiedler et al., 2003) and radiation waves (Stahl and von Rohr, 2004), most non-invasive techniques utilize the optical methods to determine the sheet thickness.

The light attenuation method (de Oliveira et al., 2006) determines the thickness by measuring the attenuated intensity of the light passed the liquid sheet, since the intensity attenuation is an exponential function of the thickness. However, the application of such method is challenging due to the need of calibrating the

---

* Corresponding author.
  E-mail address: junchen@purdue.edu (J. Chen).

Nomenclature

α	the reciprocal of the slope of OPD-DoC function
$\Delta\eta$	the change of the optical path difference caused by introducing the test sample
$\Delta|\gamma|$	the change of the degree of coherence caused by introducing the test sample
η	optical path difference (OPD)
η_0	coherence length of the light source
λ	wavelength of the light source
$|\gamma|$	degree of coherence (DoC)
μ	viscosity of ethanol
ϕ	phase
ρ	density of ethanol
σ	surface tension of ethanol
θ_i	impinging angle
A	amplitude of the wave function
a	interrogation window width
A^*	amplitude of the wave function as a constant near (x^*, y^*)
B	offset of the wave function
b	interrogation window height
B^*	offset of the wave function as a constant near (x^*, y^*)
D	nozzle diameter
d	thickness of the test sample
d_r	relative thickness distribution of the test sample
d_{ref}	absolute thickness of a reference point on the test sample
h	nozzle exit spacing
I	irradiance
I_1	irradiance of branch 1
I_2	irradiance of branch 2
I_{max}	local maximum irradiance near (x^*, y^*)
I_{min}	local minimum irradiance near (x^*, y^*)
K	impinging sheet constant
n	refractive index of the test sample
n_0	refractive index of the air
P_0	driven pressure of the pressure tank
r	radial distance to the impinging point
Re	Reynolds number of impinging jets
V_0	jet velocity
We	Weber number of impinging jets

Fig. 1. Schematic of film thickness measurement using the interferometer: the test sample thickness is d; the n and n_0 are the refractive indexes of test sample and air, respectively.

Fig. 2. Phase unwrapping process: (a) the recorded interference pattern; (b) the extracted phase distribution; and (c) unwrapped OPD distribution with directional ambiguity. Case 1 shows an increase trend of OPD from the origin and case 2 shows a decrease trend.

non-linear relationship between the sheet thickness and light attenuation. The laser-induced fluorescence method (Hidrovo and Hart, 2001; Greszik et al., 2011) relates the fluorescence intensity to the concentration of the dye in the liquid, which further reveals the liquid thickness. The disadvantages of this method include low signal-to-noise ratio, tedious calibration routine, and an adverse effect that the solvent dye alters the surface tension and viscosity of the test fluid.

The external light reflection method (Shedd and Newell, 1998) measures the total reflection angle to reconstruct the location of the top and bottom surfaces of the liquid sheet by assuming they are even surfaces. The laser focus displacement method (Han and Shikazono, 2009; Zhou et al., 2009), as a commonly used point-wise measurement technique, determines the thickness by measuring the maximum reflection between the top and bottom surfaces of the liquid sheet. It needs additional correction when an uneven surface is involved. Also, the scanning mechanism of this technique limits its application to a highly dynamic measurement.

A variety of interferometry techniques extract the phase distribution from the interference patterns introduced by the liquid
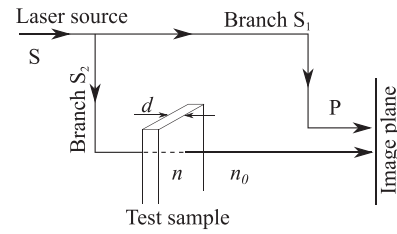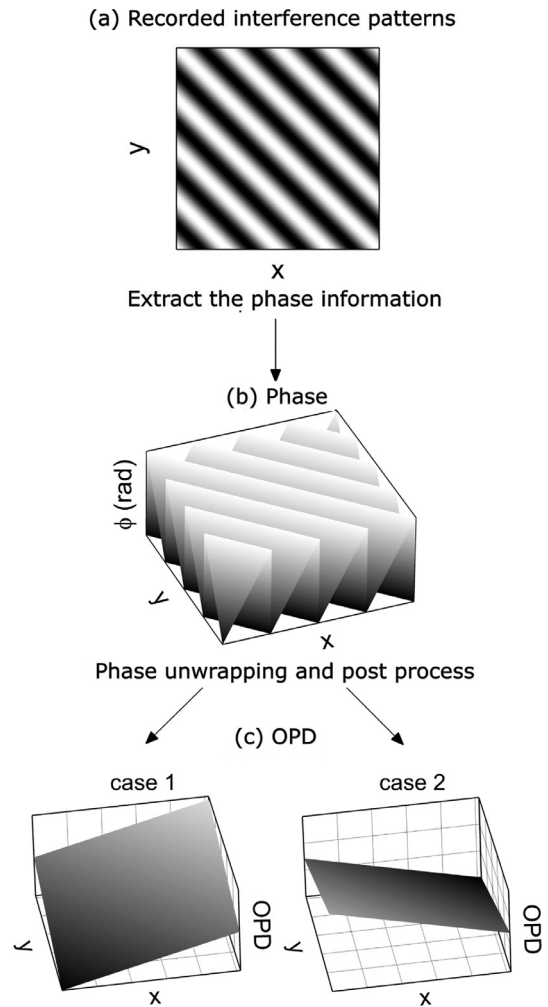
sheet and determine the thickness distribution with different additional assumptions (Nozhat, 1997; Shen and Poulikakos, 1998; van den Doel and van Vliet, 2001; Choo and Kang, 2001). For example, Choo and Kang (2001) measure the sheet thickness by combining the measured relative thickness distribution to the assumption from Taylor's model (Taylor, 1960), which claims that along a certain radial direction on the sheet,

$$d \cdot r = K, \tag{1}$$

where the d, r and K are the thickness at that location, the radial distance to the impinging point, and a constant of that radial direction, respectively. Along a radial direction, with the relative
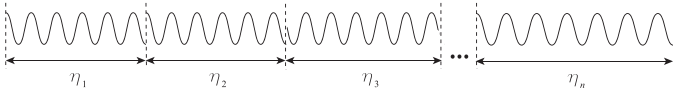
Fig. 3. A discontinuous wave train with difference lengths is emitted from a realistic laser, characterized by the coherence length $\eta_0 = \frac{1}{n}\sum_{i=1}^{n}\eta_i$.
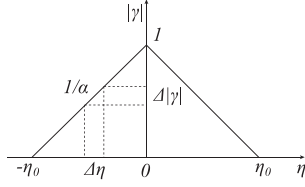

Fig. 4. The degree of coherence $|\gamma|$ as a function of the OPD η.

thickness Δd between any two points at radial distances r_1 and r_2, the constant K is determined as

$$K = \Delta d / \left(\frac{1}{r_1} - \frac{1}{r_2}\right). \tag{2}$$

Applying the K to the Taylor's model (Eq. (2)) again, the thickness distribution along that radial direction is then determined. However, since this assumption neglects the rim formation and droplet detachment, the measured relative thickness distributions are against the assumption itself. To avoid making additional assumptions, a combination of laser focus displacement method and interferometry method is given in Han et al. (2011), in which the liquid sheet is restricted to the sheet flows on a flat plate.

In this paper, a new method, Partial Coherent Interferometry, is developed to measure the thickness distribution of a dynamic transparent liquid sheet. The degree of coherence (DoC, $|\gamma|$) of the recorded interference pattern from an interferometer and the optical path difference (OPD, η) between the test and reference branches are linearly related. Since the refractive indexes of liquid sheet and air are different, the sheet in test branch introduces a change of the OPD ($\Delta\eta$) which is proportional to the sheet thickness. Thus, with a known refractive index of the liquid, a calibrated $|\gamma| - \eta$ relationship, and a measured change of DoC $\Delta|\gamma|$ caused by the sheet, the thickness distribution of the liquid sheet can be determined.

We apply this method to measure different samples including a solid glass, a static liquid film, and a liquid sheet generated by impinging jets, to demonstrate that it can be applied to investigate a two-dimensional thickness distribution of a liquid sheet from a highly dynamic system.

This paper is organized as follows. The principle of the new method is introduced in Section 2. Details of the experiment setup are given in Section 3. Results are presented in Section 4, followed by the conclusions and outlooks in Section 5.

2. Method

2.1. Partial Coherent Interferometry: the principle

In this work, a liquid sheet introduces additional optical path difference in one branch of an interferometer. From the recorded interference patterns, the absolute thickness of the sheet is determined in two steps: (i) the relative thickness distribution with respect to a reference point is first obtained by unwrapping the phase of the recorded interference fringes, and (ii) the absolute thickness of that reference point is determined by analyzing the DoC around that point. We term this method as *Partial Coherent Interferometry* (PCI).

2.2. Relative thickness measurement

In an interferometer (Fig. 1), the light emitted from a source is first separated into two branches: S_1 (reference) and S_2 (test). Interference fringes are observed on image plane P due to a non-zero OPD of two branches ($S - S_1 - P$ and $S - S_2 - P$). When a test sample is introduced in branch S_2, the interference pattern will changed accordingly. The irradiance of interference pattern is

$$I(x, y) = A(x, y) \cdot \cos(\phi(x, y)) + B(x, y), \tag{3}$$

where ϕ is the phase ($\phi \in [-\pi, \pi]$, $\phi = 0$ for the constructive interference and $\phi = \pm\pi$ for the destructive interference). Meanwhile, A and B are the local amplitude and offset, respectively. $\phi(x, y)$ can be extracted via a Fourier transformation method (Takeda et al., 1982). Every two adjacent fringes of $I(x, y)$ indicate an OPD of one wavelength λ. By unwrapping the $\phi(x, y)$ as shown in Fig. 2, one can get the corresponding OPD distributions. Thus, the relative thickness $d_r(x, y)$ is determined by subtracting the distribution without the test sample from the distribution with the test sample. However, the tendency of the OPD across the fringe patterns is still unclear (directional ambiguity), leaving two possibilities (increasing or decreasing) as illustrated in Fig. 2.
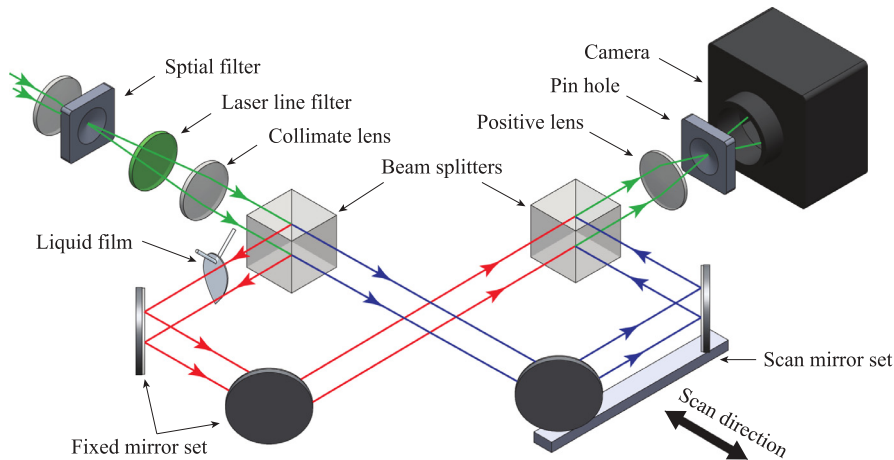

Fig. 5. Schematic of PCI setup for measuring a dynamic liquid film thickness. (For interpretation of the references to colour in this figure legend, the reader is referred to the web version of this article.)
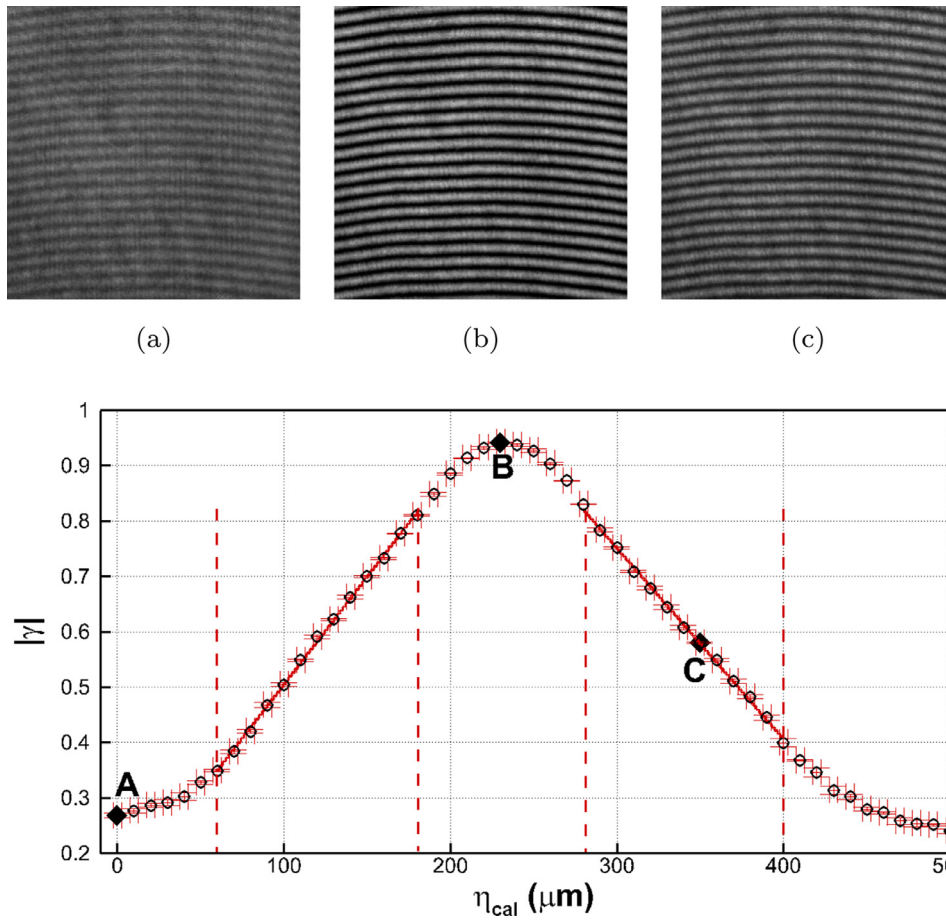
(a)   (b)   (c)

Fig. 6. $|\gamma| - \eta_{cal}$ relationship established by the calibration process. (a), (b) and (c) are the interference patterns at A ($\eta_{cal} = 0$ μm), B ($\eta_{cal} = 230$ μm) and C ($\eta_{cal} = 350$ μm), respectively. The linear regions are indicated by the red dashed lines and fitted curves. An average uncertainty for the measured DoC points is $\sim \pm 0.3\%$ and the average uncertainty for calibration OPD is $\pm 0.5\%$, shown as the vertical and horizontal error bar, respectively. (For interpretation of the references to colour in this figure legend, the reader is referred to the web version of this article.)
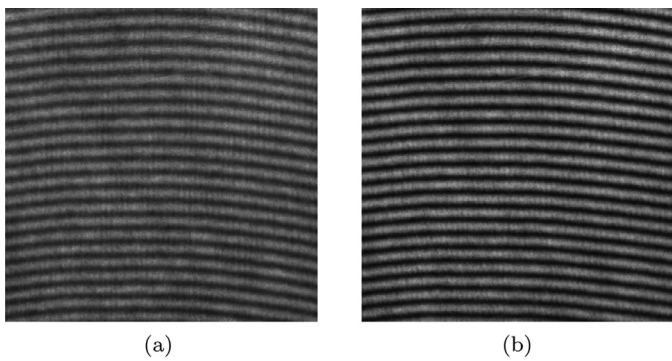

(a)   (b)

Fig. 7. The recorded interference patterns. (a) without the glass sample and (b) with the glass sample.
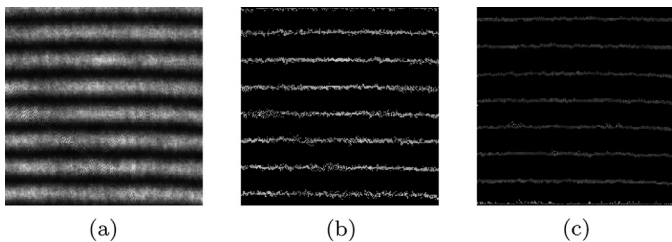

(a)   (b)   (c)

Fig. 8. Identified local maximum and minimum pixels within the interrogation window. (a) interrogation window, (b) identified local maximum intensity pixels and (c) identified local minimum intensity pixels.
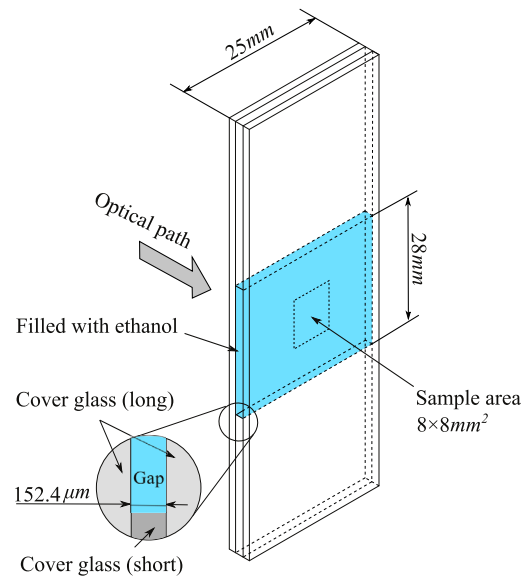

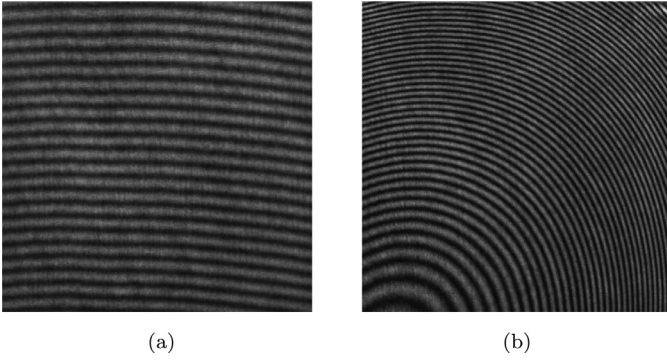**Fig. 9.** Schematic of static liquid film sample.

Fig. 10. The recorded interference patterns: (a) without the ethanol in the gap, and (b) with the ethanol in the gap.

2.3. Absolute thickness measurement

Ideally, a laser is modeled as a coherent light source which emits a continuous harmonic wave. However, in reality, as illustrated in Fig. 3, a laser emits trains of harmonic waves separated by random phase difference. This kind of partial coherent light is characterized by a coherence length η_0 defined as the average length of those finite wave trains.

When the partial coherent light is used as the light source in an interferometer, the irradiance is then (Pedrotti et al., 2007)

$$I(x, y) = I_1(x, y) + I_2(x, y) + 2\sqrt{I_1(x, y)I_2(x, y)}$$
$$\cdot |\gamma(x, y)| \cos(\phi(x, y)), \tag{4}$$

where $I_{1,2}(x, y)$ and $|\gamma(x, y)|$ are the local irradiance of $S_{1,2}$ and local DoC, respectively. As shown in Fig. 4, the local DoC also is a function of OPD (Pedrotti et al., 2007)

$$|\gamma| = \begin{cases} 1 - |\eta|/\eta_0, & \text{if } |\eta| \leq |\eta_0| \\ 0, & \text{otherwise} \end{cases}. \tag{5}$$

A complete coherent case, $\eta = 0$ and $|\gamma| = 1$, indicates two identical wave trains are superposed all the time. A complete incoherent case, $\eta > \eta_0$ and $|\gamma| = 0$, means two wave trains always superposed with a random phase difference, and thus no interference is observed. When $0 < \eta < \eta_0$, and $0 < |\gamma| < 1$, two wave trains

superposed at the (x, y) are partially coherent since the phase difference is neither a constant 0 nor totally random. Thus, the visibility of the interference pattern reflects the DoC. Since the coherent length η_0 is laser specific, the measurement range can be adjusted by choosing different lasers.

In order to use the $|\gamma| - \eta$ relationship to determine the η, by relating Eqs. (3) and (4), one gets

$$A(x, y) = 2\sqrt{I_1(x, y)I_2(x, y)} \cdot |\gamma(x, y)| \tag{6}$$

and

$$B(x, y) = I_1(x, y) + I_2(x, y). \tag{7}$$

Thus, from Eq. (6), the DoC is

$$|\gamma(x, y)| = \frac{A(x, y)}{2\sqrt{I_1(x, y)I_2(x, y)}}. \tag{8}$$

Since S_1 is not influenced by the test sample, $I_1(x, y)$ can be directly measured by recording the image while S_2 is blocked. Then, from Eq. (7), I_2 can be determined as

$$I_2(x, y) = B(x, y) - I_1(x, y). \tag{9}$$

Assuming, within a small interrogation window $\{(x, y) : x \in [x^* - a/2, x^* + a/2], y \in [y^* - b/2, y^* + b/2]\}$ centered around a reference point (x^*, y^*), $A(x, y)$, $B(x, y)$, $I_1(x, y)$, $I_2(x, y)$, and $|\gamma(x, y)|$ are local constants (denoted as A^*, B^*, I_1^*, I_2^*, and $|\gamma|^*$, respectively). In such window, the local maximum and minimum, $I_{max}(x, y)$ and $I_{min}(x, y)$, can be calculated as the averages of irradiance at $\phi(x, y) = 0$ and $\phi(x, y) = \pm\pi$, respectively. Then, we estimate A^* and B^* as

$$A^* = \frac{I_{max} - I_{min}}{2} \tag{10}$$

and

$$B^* = \frac{I_{max} + I_{min}}{2}. \tag{11}$$

Substituting A^* and B^* back into Eqs. (8) and (9), $|\gamma|^*$ is then determined

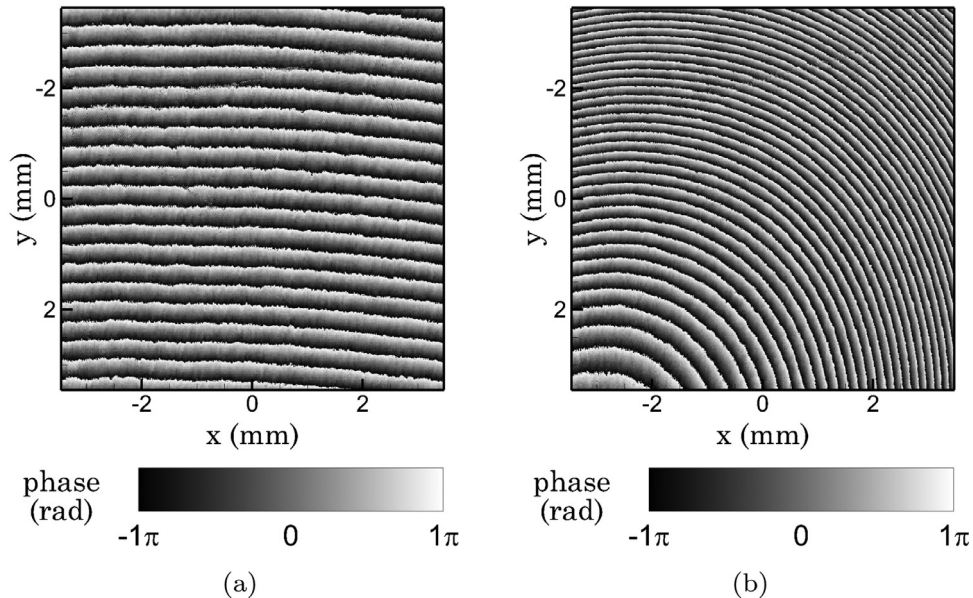$$|\gamma|^* = \frac{I_{max} - I_{min}}{2\sqrt{2I_1^*(I_{max} + I_{min} - 2I_1^*)}}. \tag{12}$$

Fig. 11. The phase distribution extracted from the recorded interference patterns: (a) without the ethanol in the gap, (b) with the ethanol in the gap.
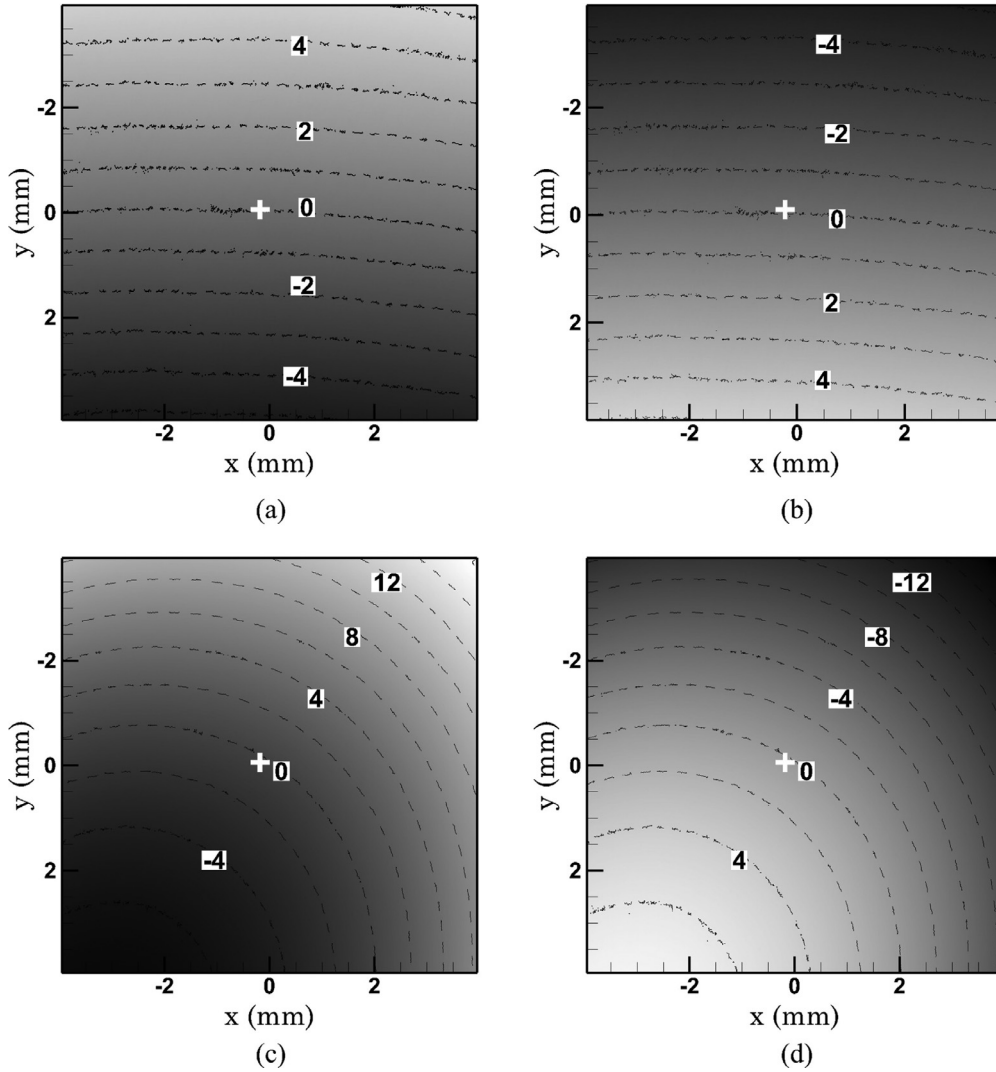
Fig. 12. Distribution of the unwrapped OPD (unit of contour labels: μm): (a) without the ethanol in the gap case 1; (b) without the ethanol in the gap case 2; (c) with the ethanol in the gap case 1; and (d) with the ethanol in the gap case 2. The plus symbols indicate the reference points where relative OPD is set to zero.

By applying Eq. (12) to process the images with and without the test sample, the DoCs at the same point in these two images are acquired. Therefore, by subtracting one from another, $\Delta|\gamma|$ caused by test sample is obtained. From Eq. (5), the change of the OPD is proportional to the change of the DoC, i.e.,

$$\Delta\eta = \alpha\Delta|\gamma|. \tag{13}$$

Here, the coefficient α is the reciprocal of the slope of the $|\gamma| - \eta$ function (Fig. 4) which can be determined from a calibration procedure individually.

One is reminded that in the introduced interferometer (Fig. 1), the absolute thickness at a reference point is related to the change of the OPD as

$$d = \Delta\eta/(n - n_0), \tag{14}$$

where n and n_0 are the refractive indexes of the test sample and the air, respectively.

Thus, one can determine the thickness of the test sample at the point (x^*, y^*) by applying the measured $\Delta\eta$ and the refractive index of the test sample to Eq. (14). Repeating this procedure at multiple points and examining the thickness distribution trend described by those points, the true relative thickness

distribution is then identified from the possibilities obtained in Section 2.2 (to overcome the directional ambiguity). Combining the identified thickness distribution and the absolute thickness at the reference point, the absolute thickness distribution of the test sample is finally retrieved.

3. Experimental setup

As shown in Fig. 5, a laser beam ($\lambda = 450$ nm, 1.6 W diode laser), is first spatially filtered and collimated. Then, it is splitted into two branches, the reference branch S_1 and the test branch S_2 indicated by blue and red in Fig. 5, respectively. The reference branch passes a scan mirror set and the test branch passes the test sample and a fixed mirror set correspondingly. Two separated beams rejoin at second beam splitter and pass through a lens and a pinhole. Eventually, a scaled interference pattern is generated on the image plane and recorded by a high-speed camera (Photron FASTCAM SA-Z 1024×1024 pixels). For calibration purpose, the scan mirror set is able to move with a minimum increment of 1 μm to adjust OPD between two branches via a translation stage. However, during the measurement, the scan mirror set stays still.
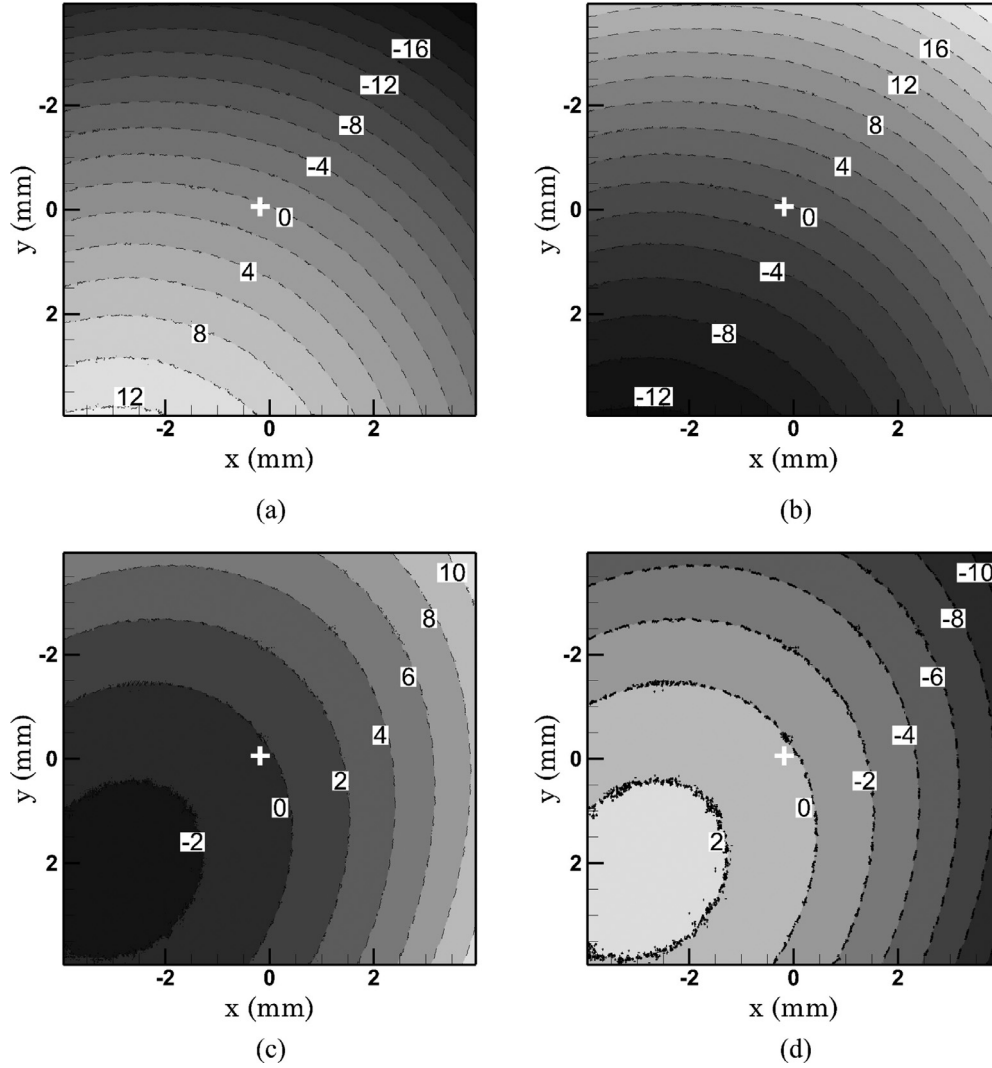
Fig. 13. Four possible OPD distributions from the results in Fig. 12 (unit of contour labels: μm): (a) Fig. 12d - Fig. 12a; (b) Fig. 12c - Fig. 12b; (c) Fig. 12c - Fig. 12a; and (d) Fig. 12d - Fig. 12b. The crosses at the center of each image indicate the reference point.

In the calibration, the scan mirror set is initially adjusted to set the calibration OPD $\eta_{cal} = 0$. As the scan mirror set translates with an interval δ, the OPD changes as twice of the scanning distance, i.e., $\Delta \eta_{cal} = 2\delta$. The corresponding $|\gamma|$ at each step is measured via Eq. (12). Then, the $|\gamma| - \eta$ relationship is established (Fig. 6) by relating those $|\gamma|$ with the scanning distance. The average uncertainty of the measured DoC is $\pm 0.3\%$. Two linear regions are identified (the dashed lines). One is reminded that there are non-linear regions located near the three vertices of the triangular curve, where the measurements should avoid. The one near the apex may be caused by the non-linear sensitivity of the CCD sensor near to its intensity measurement limit. As well as the two near the base might be caused by the low contrast of the interference pattern. However, the detailed understanding of these non-linear regions is still to be studied. The first linear region, which ranges from 60 to 180 μm with an $\alpha = 257.1 \pm 2.3$ μm determined by linear regression, is selected as the test region. At the beginning of the measurement, the scan mirror set is adjusted to ensure that the measured DoCs are all located in that linear region. Since the maximum $\Delta \eta$ should also fall into such linear region, with Eq. (14), the valid measurement ranges for ethanol and glass are $2.1 \sim 331.6$ μm and $1.5 \sim 228.4$ μm, respectively.

4. Results

The PCI method is applied to three different test samples: a solid glass sample, a static liquid film sample and a dynamic impinging sheet formed by two alike impinging jets.

4.1. Thickness of a solid sample

When a solid glass sample ($n = 1.5255$) is placed in test branch. As shown in Fig. 7, there is no noticeable change of interference pattern after the sample is inserted since the glass sample is of high flatness. To measure the thickness, an interrogation window (256×256 pixels) is applied to both images at the center. As an example, Fig. 8a shows the image enclosed by the interrogation window for the case of glass sample. By applying the process introduced in Section 2.3, the local maximum and minimum intensity pixels are identified (Fig. 8b and c). I_{max} and I_{min} are the average intensity of the these identified pixels. To estimate I_1^*, an image is recorded while test branch S_2 is blocked and thus, I_1^* is the average intensity within the same interrogation window. Substituting I_{max}, I_{min} and I_1^* to Eq. (12), the DoC for the case of glass sample is calculated. By repeating the same process to the image without
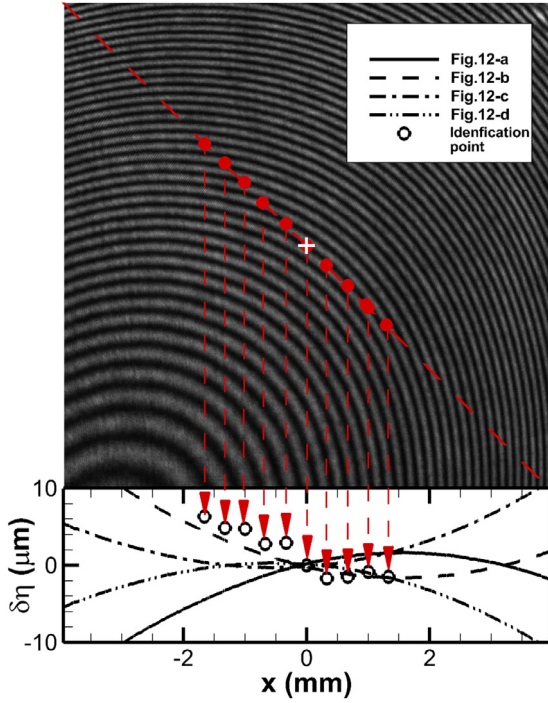
Fig. 14. Partial coherence analysis for ambiguity identification around the reference point. Ten ambiguity identification points indicated by the red dots located on the diagonal. The OPDs relative to the reference point ($\delta\eta$) for identification points are shown as the circles in the plot at the bottom. Also plotted are four possible types of OPD distributions along that diagonal in Fig. 13a–d for comparison. (For interpretation of the references to colour in this figure legend, the reader is referred to the web version of this article.)
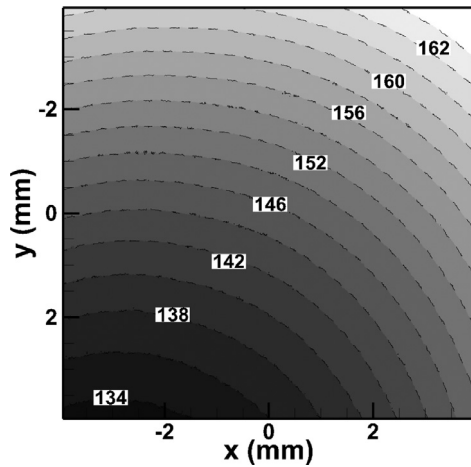

Fig. 15. Thickness distribution of static ethanol film (unit of contour labels: μm).

the glass sample, the change of DoC $\Delta|\gamma| = 0.304 \pm 0.001$ is measured. With the calibrated $\alpha = 257.1 \pm 2.3$ μm, the change of OPD is calculated as

$$\Delta\eta = \alpha \cdot \Delta|\gamma| = 78.2 \pm 1 \ \mu m.$$

Then, with Eq. (14), the thickness d_m is

$$d_m = \frac{\Delta\eta}{n - n_0} = 148 \pm 1.8 \ \mu m,$$

while the repeated measurements using a caliper give 152.4 ± 1.3 μm.
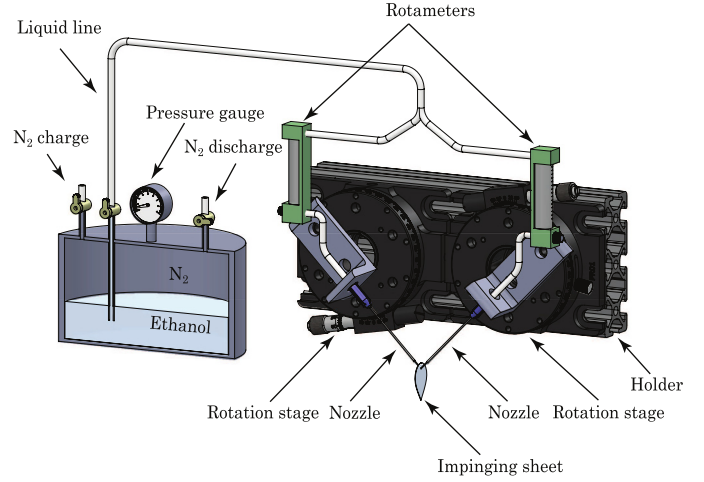

Fig. 16. Schematic of dynamic liquid film generated from two impinging jets with an alike angle 90°.
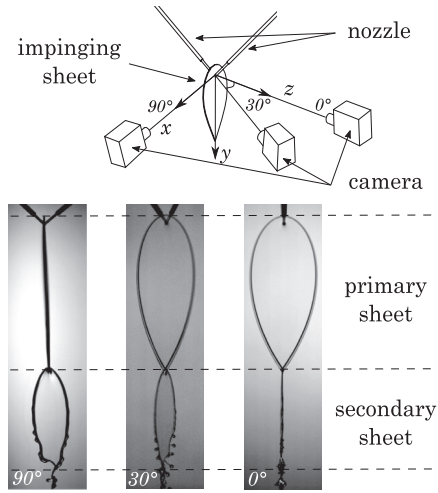

Fig. 17. Impinging sheet observed at 0°, 30° and 90°.

4.2. Thickness of a static liquid film

A static liquid film sample is made by filling ethanol ($n = 1.3619$) into a gap formed by four pieces of glass (Fig. 9). The nominal thickness of the gap is 152.4 μm measured by a caliper. The recorded interference patterns before and after the injection of the ethanol are shown in Fig. 10. The thickness of the liquid film is not uniformly distributed in the gap due to the effects of surface tension and gravity. The sample area is about 8×8 mm^2, located at the center of the gap region.

By applying the procedure introduced in Section 2.2, the phase distributions and the corresponding unwrapped OPD distributions are given in Figs. 11 and 12, respectively. One is reminded that, because of directional ambiguity, the unwrapped OPD for each image has two possible results as shown in Fig. 12. The reference points for two unwrapping results are denoted as the cross symbols located at (0,0). Then, the OPD caused by the ethanol film is calculated by subtracting the unwrapped OPD without the film from the one with the film. As shown in Fig. 13, this operation results four possible OPD distributions, and the one representing the true thickness distribution is to be identified. To solve this directional ambiguity problem, the absolute thicknesses of a series of
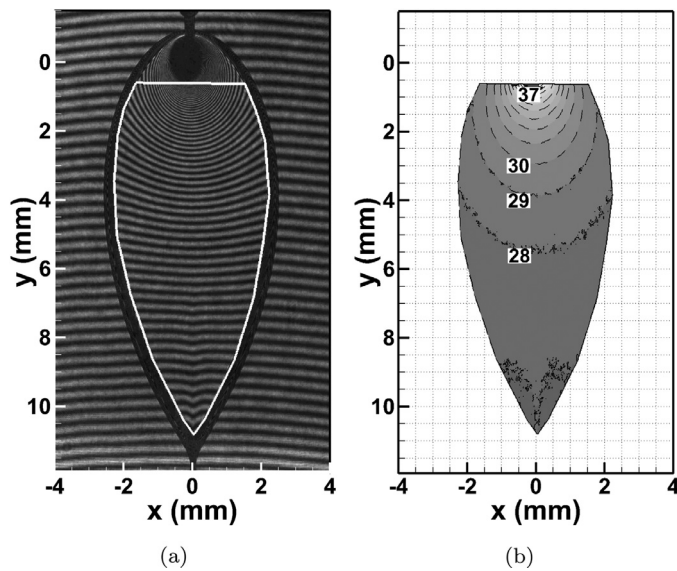
Fig. 18. (a) A typical snapshot of the interference pattern with the thickness interrogation area highlighted, (b) the thickness distribution measured via PCI from the interference pattern of (a) (unit: μm).

Table 1
Conditions of the impinging jet experiment.

parameter	value
driven pressure P_0 (kPa)	69
nozzle diameter D (mm)	0.25
impinging angle θ_i (°)	45
nozzle exit spacing h (mm)	2
refractive index n	1.3619
fluid viscosity μ (Pa $\cdot$ s)	1.040×10^{-3}
fluid density ρ (kg/m^3)	789.3
surface tension σ (N/m)	2.239×10^{-2}
jet velocity V_0 (m/s)	4.02
Reynolds number $Re = \rho \cdot V_0 \cdot D/\mu$	763
Weber number $We = \rho \cdot V_0^2 \cdot D/\sigma$	143

4.3. Thickness of a impinging sheet

A dynamic liquid sheet is generated from two alike impinging jets (Fig. 16). Nitrogen in a pressure tank (gauge pressure ∼69 kPa) drives the ethanol ($n = 1.3619$) through the rotameters and nozzles. Two jets are formed at the tips of the nozzles. The details of experiment are summarized in Table 1.

A set of high-speed images (20,000 fps) are first recorded from different observation perspectives to visualize the sheet structure. As shown in Fig. 17, a primary sheet is first formed with leaf shape and there is no droplet detachment observed from the surrounding rims. By the impingement of the rims under the primary sheet, a secondary sheet is developed perpendicularly to the primary sheet with a smaller size. At the tail region of the secondary sheet, the rims become unstable and further break up into droplets.

To measure the thickness of the impinging sheet via PCI, the impinging sheet is placed in the test branch and the interference patterns are recorded. Due to the limitation of the field of view, only the primary sheet region is measured. A representative snapshot of the recorded interference pattern for the primary sheet is shown in Fig. 18a. One may note that the dark region observed near the impinging point, around ($x = 0$, $y = 0$), is formed due to the large thickness variation. The interrogation region to be analyzed by PCI for thickness measurement is enclosed by the white curve where the sheet is spanned. 1,000 images are recorded by the high speed camera with a recording rate of 20,000 fps and an exposure time of 5 μs. The measured thicknesses at the reference point ($x = 0$ mm, $y = 4.5$ mm) within this 50 ms period are shown in Fig. 19. The interrogation window is 128×128 pixels

identification points are measured via the method in Section 2.3 (Fig. 14). To compare with the relative thickness obtained from phase unwrapping process, the thickness of each identification point relative to the reference point is analyzed by subtracting the absolute thickness of the reference point from the one of identification points. By comparing the relative thicknesses obtained from the phase unwrapping process and the one from identification points, the correct relative thickness is identified as the one in Fig. 13b.

The film thickness at the reference point is $d_{ref} = 154.6 \pm 2.1$ μm. By combining the identified relative thickness distribution with the absolute thickness at the reference point, the absolute thickness distribution is determined, as shown in Fig. 15. It varies from 134 to 164 μm in the sample area. The total uncertainty includes the one from both relative thickness measurement and the absolute thickness measurement. The uncertainty of the phase unwrapping is $\lambda/2 = 0.225$ μm and the overall uncertainty for measurement of the ethanol liquid film is ∼±2.3 μm.
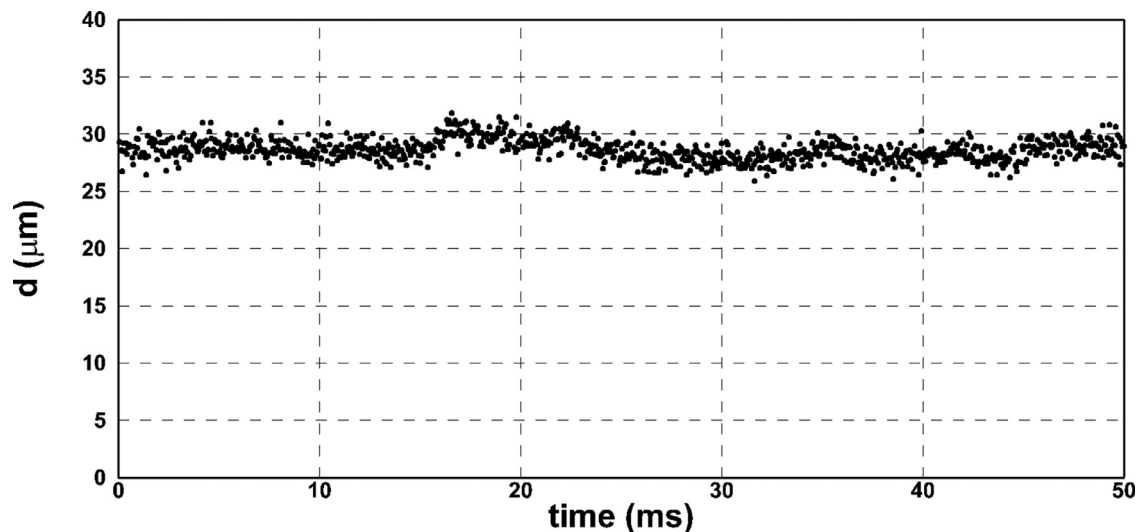

Fig. 19. The measured thickness at reference point ($x = 0 mm, y = 4.5$ mm) as a function of time.
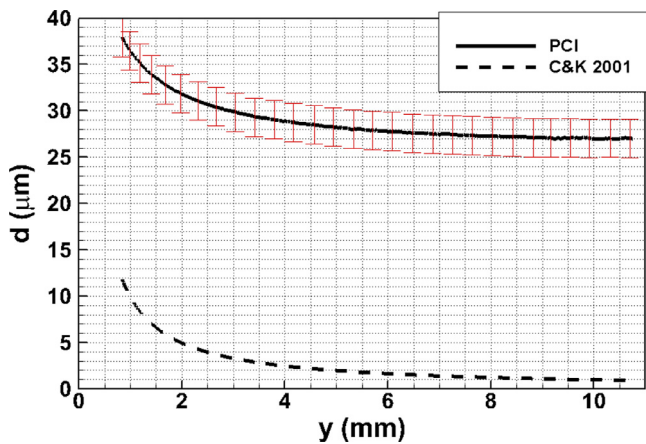
Fig. 20. The average thickness along $x = 0$ measured by PCI and the method in Choo and Kang (2001). The error bars for PCI results indicate a 95% confidence level.

centered at the reference point. The measured thicknesses at the reference point is 28.6 ± 1.8 μm. The uncertainty is twice of standard deviation of the data points shown in Fig. 19, corresponding to a confidence level of 95%. A corresponding snapshot of the thickness distribution is given in Fig. 18(b). The thickness gradually decreases from the impinging point along the radial direction and is symmetric with respect to the y-axis. With the measured relative thickness distribution, one of the methods introduced in Section 1 (Choo and Kang, 2001) is applied to compare with the PCI measurement. Fig. 20 compares the thickness along the y-axis measured by both methods. The error bars indicate a characteristic uncertainty $\sim \pm 2.1$ μm. There is a significant 25 μm offset between two results.

5. Summary and conclusions

In this paper, we develop a non-invasive technique, Partial Coherent Interferometry, for measuring the thickness of a transparent sheet dynamically. It relates the sheet thickness to the phase and the degree of coherence of the interference pattern. The test sample is placed in the test branch of an interferometer, and the interference pattern induced by the test sample is digitally recorded. There are three subroutines for implementing PCI to process the recorded interference pattern:

1. The phase of the interference pattern is extracted firstly. By unwrapping the extracted phase, the corresponding relative thickness distributions are measured. Meanwhile, the directional ambiguity problem emerges.
2. By applying the measured change of the degree of coherence caused by inserted test sample to the relationship established by the calibration, the change of optical path difference is acquired. Then, with the known refractive index of the test sample, the absolute thicknesses at the reference point and identification points are determined.
3. By matching the thicknesses of the identification points to the possible relative thickness, the problem of directional ambiguity is solved. Furthermore, by combining the absolute thickness at the reference point and the identified relative thickness distribution, the absolute thickness distribution is determined.

In this work, the linear relationship between the optical path difference and degree of coherence decoded from the interference pattern is first verified via a calibration process. Then, PCI is applied to measure the thicknesses of a solid glass sample, a static liquid film sample, and an impinging sheet formed by impinging jets, respectively, to demonstrate its capability for measur-

ing the thickness of a uniform, curved, and/or time varying sheet. The characteristic uncertainty is ± 1.8 μm for a solid glass sample with uniform thickness, ± 2.3 μm for static liquid film sample, and ± 2.1 μm for the impinging sheet, respectively. By combining with high speed image recording, PCI can be used to measure the sheet thickness of a highly dynamic process.

The relative uncertainty of the degree of coherence measurement and the calibrated slope of the $|\gamma| - \eta$ relationship (e.g., the one shown in Fig. 6) are $\pm 0.3\%$ and $\pm 1\%$, respectively. In general, the overall uncertainty is mainly determined by the uncertainty of the measured degree of coherence, the calibrated slope ($1/\alpha$) and the phase unwrapping process. In particular: (i) The interrogation area for the degree of coherence measuring affects the uncertainty predominantly. A larger data area contains more interference pattern, leading to a possible higher accuracy since the number of statistical samples to estimate the degree of coherence is increased. However, an increased area results in smoothing the local thickness variance and thus, it might lead to a decreased accuracy where the local thickness variation is significant. To reconcile this contradiction, the interrogation area should be selected such that the relative thickness in this area displays less variation. (ii) The slope coefficient α affects the resolution of the measurement. Using a laser with shorter coherence length will increase the accuracy because the same $\Delta|\gamma|$ resolves a smaller $\Delta\eta$. However, this will reduce the measurement range. It is thus possible to select the measurement range by choosing different lasers. (iii) The smaller the refractive index difference between the test sample and the air is, the larger the uncertainty increases.

The accuracy of PCI is also influenced by factors such as the incident angle on the surface, the attenuation of the light after passing through the sample, and the reflection on the interface. In this paper, it is assumed that the laser beam is of normal incidence to the test sample surface. This can be satisfied by careful alignment of the optical system. However, an offset of incident angle will lead to an additional error. For example, a 5-degree incident angle on a 100 μm thick sample will result in an extra error of 0.4 μm. From Eq. (9), the light intensity after passing the test sample (I_2) is determined in PCI, thus the laser attenuation and reflection will not affect the measurement results. This represents another advantage of the PCI.

In the present work, the PCI is developed with a 450 nm continuous wave laser. Since the interference patterns are recorded by high-speed camera with an exposure time of 5 μs and a recording frame rate of 20,000 fps, the current design is able to measure the dynamic change of the sheet thickness. Adopting a pulse laser in this PCI system will further expand its capacity to measure highly dynamic process (effective exposure time ~ 10 ns). A systematic study is needed to tackle the challenge of calibration and pulse to pulse intensity variation which should be addressed in future work.

Supplementary material

Supplementary material associated with this article can be found, in the online version, at doi:10.1016/j.ijmultiphaseflow.2019.04.002.

References

Bayvel, L.P., 1993. Liquid Atomization. Taylor & Francis, Washington, DC.
Chojnacki, K., 1997. Atomization and mixing of impinging non-newtonian jets. The University of Alabama in Huntsville ProQuest Dissertations Publishing.
Choo, Y.J., Kang, B.S., 2001. Parametric study on impinging-jet liquid sheet thickness distribution using an interferometric method. Exp. Fluids 31 (1), 56–62.
Couto, H., Bastos-Netto, D., 1991. Modeling droplet size distribution from impinging jets. J. Propul. Power 7, 654–656.
van den Doel, L.R., van Vliet, L.J., 2001. Temporal phase-unwrapping algorithm for dynamic interference pattern analysis in interference-contrast microscopy. Appl. Opt. 40 (25), 4487–4500.

Fiedler, S., Yildiz, S., Auracher, H., 2003. Determination of film thickness and flooding during reflux condensation in a small, inclined tube with an ultrasonic transducer. Int. J. Energy Res. 27 (4), 315–325.

Fukano, T., 1998. Measurement of time varying thickness of liquid film flowing with high speed gas flow by a constant electric current method (cecm). Nucl. Eng. Des. 184 (2), 363–377.

Greszik, D., Yang, H., Dreier, T., Schulz, C., 2011. Laser-based diagnostics for the measurement of liquid water film thickness. Appl. Opt. 50 (4), A60–A67.

Han, Y., Shikazono, N., 2009. Measurement of liquid film thickness in micro square channel. Int. J. Multiphase Flow 35 (10), 896–903.

Han, Y., Shikazono, N., Kasagi, N., 2011. Measurement of liquid film thickness in a micro parallel channel with interferometer and laser focus displacement meter. Int. J. Multiphase Flow 37 (1), 36–45.

Hasson, D., Peck, R.E., 1964. Thickness distribution in a sheet formed by impinging jets. AIChE J. 10 (5), 752–754.

Hidrovo, C.H., Hart, D.P., 2001. Emission reabsorption laser induced fluorescence (erlif) film thickness measurement. Meas. Sci. Technol. 12 (4), 467.

de Jong, P., Gabriel, K.S., 2003. A preliminary study of two-phase annular flow at microgravity: experimental data of film thickness. Int. J. Multiphase Flow 29 (8), 1203–1220.

Kang, B.S., Shen, Y.B., Poulikakos, D., 1995. Holography experiments in the breakup region of a liquid sheet formed by two impinging jets. Atomization Sprays 5 (4&5), 387–402.

Li, R., Ashgriz, N., 2006. Characteristics of liquid sheets formed by two impinging jets. Phys. Fluids 18 (8), 087104.

Miller, K.D., 1960. Distribution of spray from impinging liquid jets. J. Appl. Phys. 31 (6), 1132–1133.

Nozhat, W.M., 1997. Measurement of liquid-film thickness by laser interferometry. Appl. Opt. 36 (30), 7864–7869.

de Oliveira, F.S., Yanagihara, J.I., PacÃfico, A.L., 2006. Film thickness and wave velocity measurement using reflected laser intensity. J. Braz. Soc. Mech. Sci. Eng. 28 (1), 30–36.

Pedrotti, F.L., Pedrotti, L.S., Pedrotti, L.M., 2007. Introduction to Optics. Upper Saddle River, N.J.: Pearson Prentice Hall.

Shedd, T.A., Newell, T.A., 1998. Automated optical liquid film thickness measurement method. Rev. Sci. Instrum. 69 (12), 4205–4213.

Shen, Y.-B., Poulikakos, D., 1998. Thickness variation of a liquid sheet formed by two impinging jets using holographic interferometry. ASME. J. Fluids Eng 120 (3), 482-487.

Shiina, K., Nakamura, S., Narita, K., Mori, H., Yasunari, S., 2000. Cooling characteristics of an impinging spray jet which forms an ellipsoidal liquid film. Heat Transfer Asian Res. 29 (4), 280–299.

Stahl, P., von Rohr, P.R., 2004. On the accuracy of void fraction measurements by single-beam gamma-densitometry for gas–liquid two-phase flows in pipes. Exp. Therm Fluid Sci. 28 (6), 533–544.

Sutton, G.P., Biblarz, O., 2017. Rocket Propulsion Elements, 9th edition. Wiley.

Takeda, M., Ina, H., Kobayashi, S., 1982. Fourier-transform method of fringe-pattern analysis for computer-based topography and interferometry. J. Opt. Soc. Am. 72 (1), 156–160.

Taylor, G., 1960. Formation of thin flat sheets of water. Proc. R. Soc. London A 259 (1296), 1–17.

Zhou, D., Gambaryan-Roisman, T., Stephan, P., 2009. Measurement of water falling film thickness to flat plate using confocal chromatic sensing technique. Exp. Therm. Fluid Sci. 33 (2), 273–283.